Grain size control of crystalline III-V semiconductors at ambient conditions using electrochemically mediated growth

Marco Valenti,[a†] Yorick Bleiji, [a†] Loreta A. Muscarella,[a] Mark Aarts[a] and Esther Alarcón Lladó[a*]

Center for Nanophotonics, AMOLF Institute, Amsterdam, The Netherlands

III-V semiconductor family has composition and size dependent optoelectronic properties ideal for a variety of applications in photonics and electronics. Due to the ever-increasing demand for nanophotonic and nanoelectronic devices, new crystal growth techniques have been proposed to tackle economical disadvantages of the more traditional methods. Electrochemical mediated III-V crystal growth has been demonstrated at room temperatures and pressures. One of the ad-vantages of this technique is the possibility of controlling the crystal growth with the applied potential. In this work we study the relationship between the applied potential and the resulting crystal structure of InAs. Raman analysis shows that the average crystal correlation length of the electrochemically grown InAs can be tuned by the deposition potential. In particular, we find that the average correlation length decreases with applied potential, following the phonon confinement model. The decrease in the average crystal correlation size is explained here by an increase in the nanostructured roughness of the grown InAs. Such roughness is likely induced by co-contaminant gas evolution (e.g., H_2 and AsH_3) and/or As overgrowth. Our results clearly show that the crystal structure of electrochemically grown III-V semiconductors can be controlled with the potential, opening up the possibility to fine-tune optoelectronic properties at atmospheric conditions.

Introduction

III-V semiconductors exhibit exceptional (opto)electronic properties, which makes them ideal functional materials in photovoltaics,[1–4] photoelectrochemistry,[5–7] light sensors,[8–10] light sources[11] and high speed devices.[12,13] The growth mechanisms of III-V semiconductors in the vapour phase have been extensively studied,[14–16] shedding light on the effect of growth parameters on the strain, crystallinity and impurities. Common vapour phase growth methods, such as metal-organic vapour phase epitaxy (MOVPE)[17] and molecular beam epitaxy (MBE)[14,16], have already demonstrated high quality layers in terms of crystallinity and purity. However, these techniques require expensive equipment due to their operational conditions (i.e., high temperatures and ultra-high vacuum).

More recently, a new solution-based method has been demonstrated to grow covalent crystals under ambient pressure conditions and at temperatures below 100 C.[18,19] This method, called electrochemically mediated growth, combines electrochemical deposition and solid state alloying. In the case of III-V semiconductors, one of the elements (e.g., As) is electrochemically deposited from an electrolyte solution onto a substrate that is made out of the second bimetallic component (e.g., In). Upon electrochemical deposition a solid-state reaction takes place that forms the bimetallic compound.

The potential of this method to fabricate new III-V-based optoelectronic devices lies at its easy implementation (i.e. just a beaker and a current/potential source), material composition tuneability (either by co-deposition or by using an alloy as metal substrate) and bottom-up nanostructuring. Regarding the latter, spatial selectivity on pre-patterned substrates with an insulating mask is intrinsic to electrodeposition, given that it exclusively occurs at conducting regions.[20,21] In particular, control over size and periodicity of semiconductor nanostructure arrays are key parameters in the new generation of electronic and photonic devices.

Despite the strong potential of the electrochemically mediated growth of III-V to fabricate films and nanostructures in a cost-effective manner, the technique is still at its infancy. Particularly, the growth mechanisms are not fully understood and the influence of the electrochemical parameters on important semiconductor properties, such as crystal quality, has not been elucidated. One key parameter in electrochemical deposition is the applied potential, a fine tuning knob for stoichiometry, crystal structure and growth rate that does not exist in any other synthetic method.

In this work we report the growth and characterisation of InAs nanostructures as a platform to understand the macroscopic electrochemically mediated growth of III-V semiconductors. We use Raman spectroscopy as means to probe the crystal quality and grain size as a function of deposition potential. We find that the average InAs grain size systematically decreases with increasing the cathodic voltage (from ~30 to ~10 nm), particularly after a certain critical potential. We explain our findings by the interplay between self-diffusion in the solid-state reaction rate, the voltage-dependent deposition rate and activation of spurious electrochemical reactions. This finding opens up the possibility to control the crystal grain size with potential to optimize the optoelectronic properties for specific applications. Even though we have used InAs as platform, our results can be used as guideline for the optimization of other III-V bimetallic compounds.

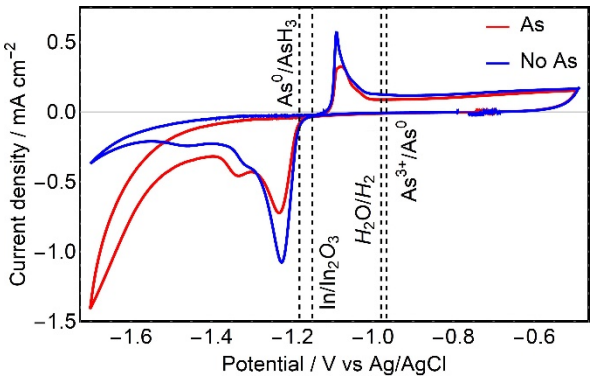

Figure 1. Cyclic voltammogram of an In foil in a solution with 0.78 mM As^{3+} and without As precursor. All the measurements were carried out at pH 13 with a supporting electrolyte (0.1 M Na_2SO_4 and 0.1 M NaOH). The vertical dashed lines are the redox thermodynamic potentials for As deposition, hydrogen evolution, In_2O_3 reduction and arsine evolution at the experimental conditions.

Results

We investigate the electrochemically mediated growth of InAs by applying a cathodic potential to an In foil in contact with an electrolyte containing As^{3+} ions. Electron back scattering diffraction (EBSD) maps of the bare In foil identify single crystalline domains as large as ~ 200 μm (see supplementary information S1 for details on the EBSD analysis).

To determine the potential window for As deposition, we assess the electrochemical processes occurring at the In-electrolyte interface by comparing the current-voltage response in cyclic voltammetry (CV) for electrolytes with and without As precursor (Figure 1). The vertical dashed lines in Figure 1 correspond to estimated redox thermodynamic potentials of some expected reactions (for detailed calculation of the potential values see supplementary information S2). All potentials in this manuscript are referenced to Ag/AgCl.

The cathodic sweeps in Figure 1 clearly show a reduction peak at ~ -1.22 V (followed by two smaller peaks) for both electrolytes. These features are in good agreement with the reduction of In_2O_3 to In. At more cathodic potentials the current exponentially increases, with the absolute current density being higher for the electrolyte containing As ions. We attribute this fast increase in current to the H_2 evolution reaction ($V_{H2O/H2}$= -0.957 V). The additional current for the As-containing electrolyte is likely due to the reduction of As^{3+} into As solid ($V_{As3+/As}$= -0.938 V):

$$As^{3+} + 3\,e^- \xrightarrow{k_1} As(0) \qquad \text{Eq. 1}$$

and possibly the further reduction of As(0) into Arsine gas ($V_{As/AsH3}$= -1.182 V).

$$As(0) + 3H^+ + 3\,e^- \xrightarrow{k_2} AsH_3 \qquad \text{Eq. 2}$$

Here, k_i are the reaction rates, that are regulated by the applied potential.

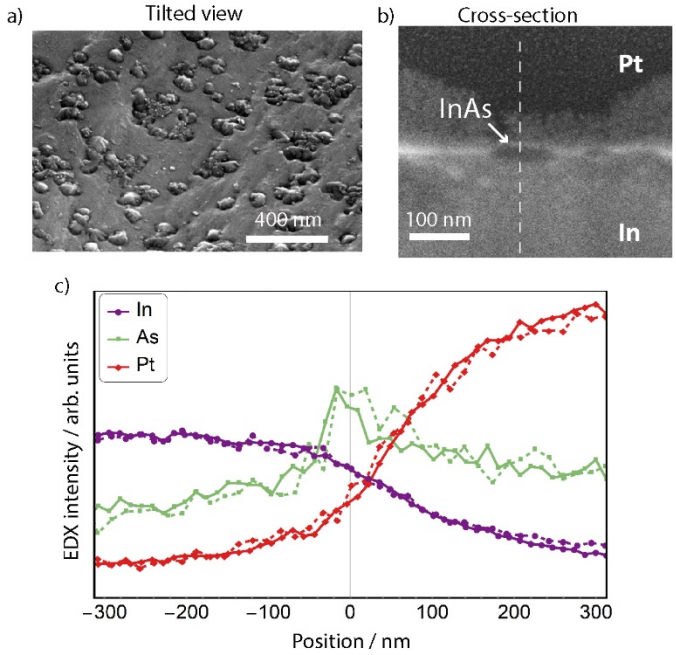

Figure 2. a) Tilted SEM image of the as-grown sample at V = -1.25 V. b) Cross-section SEM image across a nano-island for the sample grown at -1.175 V. c) EDX chemical composition profile along the dashed line in (b). Data connected with dotted lines correspond to data obtained for an equivalent line profile in the sample grown at -1.35 V. The central position is an estimate of the In surface.

On the other hand, the anodic sweeps show a non-negligible cathodic current for both electrolytes up to the point in which In oxidizes back ($V_{In/In2O3}$ = -1.15 V). In order to prevent the oxidation of the substrate, As deposition in this work is performed at potentials more cathodic than $V_{In/In2O3}$ with careful control; namely, -1.175V, -1.212V, -1.25V, -1.275V, -1.3V, -1.325V, -1.34V and -1.35V.

The growth of InAs is carried out by applying a fixed potential to the In foil for a fixed time lapse (90 min), after having removed the oxide layer with a cathodic sweep (see experimental section). SEM images of as-grown samples (Figure 2a and Figure S3) reveal the appearance of crystal-like protruding nano-islands for all applied potentials, that were not present on the bare substrate. The morphology is also confirmed by atomic microscopy (AFM, see Figure S4). The size of the nano-islands is similar for all samples and varies from a few tens to a few hundred nanometers. EDX maps (Figure S3) of the top surface reveal the presence of As, which predominates in the nano-islands. Figure 2b shows the SEM image of a cross section across a nano-island for the sample grown at -1.175 V. We observe a clear Z-contrast that extends to ~40 nm in thickness. Again, we find similar island dimensions in samples grown under different potential conditions. Figure 2c shows the EDX peak intensity for different chemical elements along the nano-island (dashed line in Figure 2b), and it reveals that As is mostly contained within the nano-island and it becomes negligible outside (see also supplementary information S6). We compare the EDX linescans for the samples grown with the least and most cathodic potentials (i.e., -1.175 V, solid curve, and -1.35 V, dashed curve) and they are virtually the same.

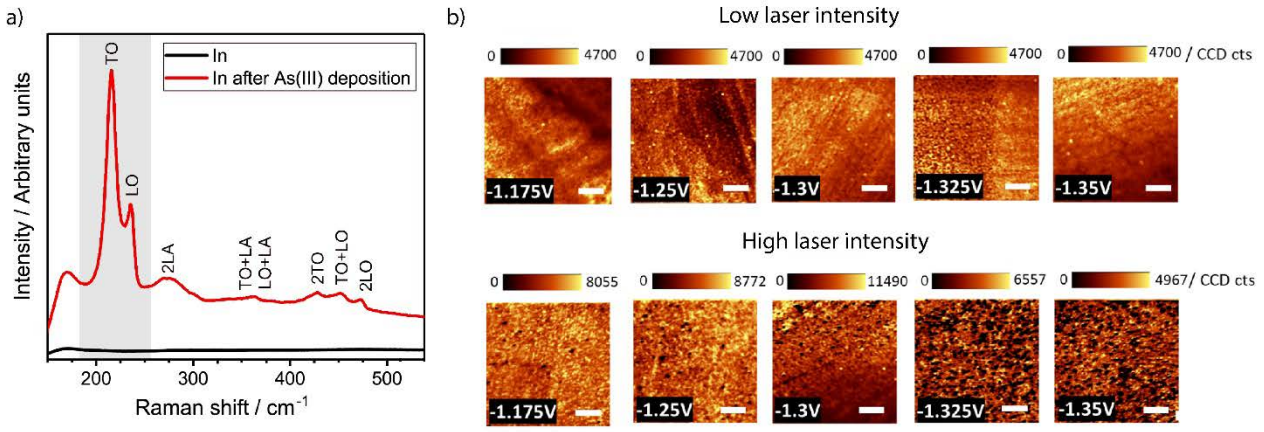

Figure 3. a) Raman spectra of an In foil before and after the electrochemical deposition of As at -1.25 V. The feature at ~170 cm^{-1} is an artefact from the long pass filter. b) Raman maps for As electrodepositions on In foils at different applied potentials with low laser intensity (top) and high laser intensity (bottom). The colour of the pixels represents the total amount of CCD counts within the shaded frequency range in a). TO and LO counts are found in all the pixels for all potentials with low laser intensity, while for high laser intensities dark spots with no InAs LO and TO counts appear.

From the integrated deposition current one can estimate an upper limit to the InAs thickness (see supplementary information Figure S2), by assuming (i) 100% faradaic efficiency for the reaction shown in Eq 1, (ii) a homogenous deposition throughout a perfectly flat substrate and (iii) full conversion of As(0) into stoichiometric InAs given that As reacts with In at room temperature[18] (see supplementary information S3). We obtain an estimated film thickness of ~ 50 nm regardless of the applied potential, which is much larger than the 40 nm thick nano-islands observed by SEM. Therefore, we suspect that significant contaminant current occurs during deposition due to hydrogen and/or arsine evolution.

To assess the formation of InAs, we probe the as-grown samples with Raman spectroscopy. Figure 3a shows a representative Raman spectrum of a sample before and after deposition of As^{3+} at -1.25 V. The details regarding the Raman set-up are described in the experimental section. Two clear prominent Raman peaks appear at ~ 216 cm^{-1} and ~ 236 cm^{-1} after deposition of As. These values are in very good agreement with the TO and LO phonon frequencies of InAs at the centre of the Brillouin zone,[22] undoubtedly identifying the presence of crystalline InAs. We also observe additional features at higher frequencies, all of which correspond to InAs second-order peaks,[22] as labelled in Figure 3a. We observe the presence of crystalline InAs Raman features in all samples grown at different potentials (Figure S7).

In order to gain information on the micron-scale homogeneity of the InAs growth as a function of applied potential, Raman maps are shown in Figure 3b for samples grown at a few potentials. The colour of each pixel represents the sum of the CCD counts under the TO and LO peaks (from 180 to 260 cm^{-1}), indicated by the grey shade in Figure 3a. At low laser intensities (top row) it is worth noting that every pixel in all maps exhibit the characteristic first-order InAs Raman peaks. Therefore, we conclude that InAs is grown all over the surface for all applied potentials within the diffraction limited resolution of the Raman map (i.e., ~ 240 nm). Despite small inhomogeneities in intensity, a quantitative assessment on the InAs thickness is not straightforward since (i) the Raman peak intensities also depend on the crystal orientation and (ii) the probing depth with 532 nm laser is limited to < 20 nm.

Surprisingly, when Raman maps were created with a higher laser intensity (bottom row in Figure 3b), a clear trend emerges as a function of potential. More specifically, we observe the presence of dark spots (i.e. no InAs signal), the density of which increases with potential. A typical Raman spectrum at the dark spot is shown in Figure S8, where a broad band appears and is typically found in amorphous As and As_2O_3.[23] The light-induced heating and decomposition of InAs into amorphous and oxide compounds has been previously reported in the literature.[24,25] This phenomenon particularly emerges in nanostructured materials, where enhanced light absorption and less efficient heat transport may occur.[26–29] Thus, the progressive decomposition of InAs with deposition potential is a first indication of decreased crystal size at high voltages and it is further discussed in the next section.

Next we focus on the crystal quality by carefully analysing the first order Raman peaks' lineshape. Figure 4a shows the measured spectra (i.e., data points) for the InAs samples grown at -1.3V, -1.325V and -1.35V. Each spectrum in Figure 4a is the average of all pixels in the corresponding low intensity Raman maps (shown in Figure 3). A Lorentzian fit to the data is also plot, where an asymmetric lineshape is considered for the LO peak (see fitting details in the experimental section). By comparing the spectra, we see a clear red shift and broadening of the LO peak with increasing potential, while the TO peak barely changes. The fact that the TO peak is stable in peak position rules out any strain differences between samples.

Figure 4b summarizes the measured LO peak position (relative to the bulk LO reference $\omega_{LO,Bulk}$ = 237.6 cm^{-1})[30] and linewidth (full width at half maximum, Γ) for all samples grown at different applied potentials. Here, each data point represents the mean value from the fitted and deconvoluted LO peak in 10 points within each sample. We observe a clear correlation between the LO peak shift and its broadening, that can be explained by phonon confinement.

In a perfect crystal, momentum conservation restricts the inelastic scattering of light by phonons to the centre of the Brillouin zone. However, if the crystal is smaller than ~ 20 atomic cells the phonon wavefunction is constrained in space. Confinement-induced uncertainty of the crystal momentum

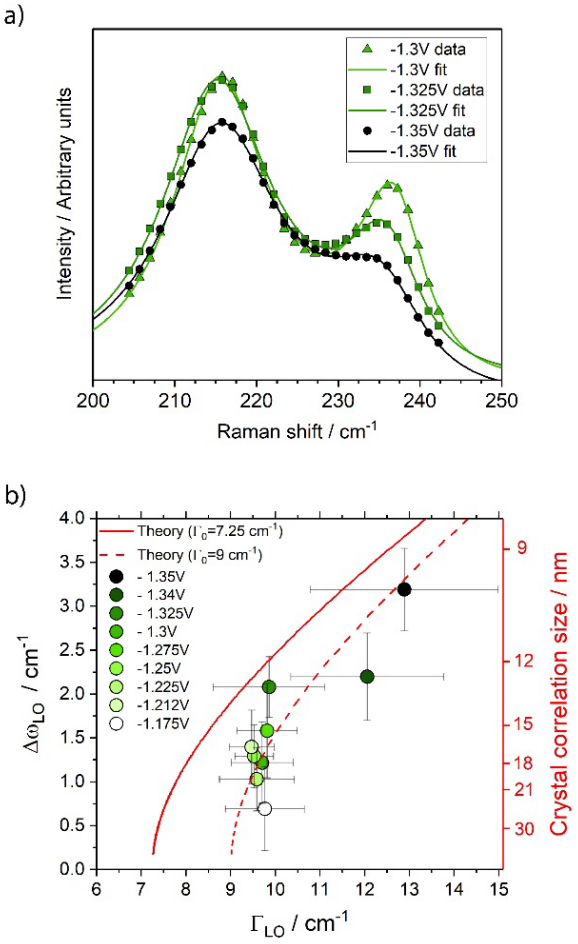

Figure 4. a) Averaged Raman spectrum for samples grown at three different potentials. Each spectrum corresponds to the average among all pixels in the corresponding low intensity Raman map shown in Figure 4. A symmetric and asymmetric Lorentzian functions are used to fit the TO and LO peaks, respectively. b) LO Raman peak shift as a function of its linewidth as predicted by Eq. 3 (solid and dashed red lines), together with the Raman shift and linewidth of single point spectra of InAs samples synthesized at different applied potentials. The standard deviation bars are given by statistics from different sample locations.

relaxes the momentum conservation rule and enables access to phonons with larger momentum. In most zinc-blende materials, only the LO phonon has a strong enough dispersion that results in a characteristic asymmetric peak broadening and red-shift with confinement. The confinement effect can be thus quantified from the lineshape of the first order Raman peaks and the phonon dispersion through the spatial correlation model.[31] This model assumes that the phonon wavefunction is spatially constrained in a sphere and predicts the following size-dependent Raman lineshape:

$$I(w) = \int \exp(-q^2L^2/4)\frac{d^3q}{[w-w(q)]^2+(\Gamma_0/2)^2} \qquad \text{Eq. 3}$$

where $w(q)$ is the phonon dispersion (see supplementary information S8 for the $w(q)$ of InAs), Γ_0 is the intrinsic LO phonon linewidth, L is the crystal correlation length and q is the phonon momentum given in units of $2\pi/a$, where a is the lattice constant (0.60583 nm for InAs).

The solid curve in Figure 4b shows the relation between the LO peak position relative to the value for bulk InAs and its linewidth as predicted by the spatial correlation model, where the intrinsic linewidth of bulk InAs is used (Γ_0 = 7.25 cm^{-1}).[30] The right-axis shows the corresponding crystal correlation size L. Figure 4b shows that the LO peak broadening and red-shift with increasing deposition potential in our samples, clearly follows the trend given by the phonon confinement model. The match is actually more obvious if a larger intrinsic phonon linewidth is used in the model (Γ_0 = 9 cm^{-1}, dashed curve). The slightly larger intrinsic linewidth, or shorter phonon lifetime, in our samples as compared to bulk InAs indicates the presence of phonon scattering potentially from non-stoichiometric defects or impurities. This relatively large intrinsic linewidth can be potentially improved by, for example, using a higher purity In substrate.

It is worth noting that all samples exhibit an estimated average grain size between ~ 10 and 30 nm, which is of the order of the observed nano-islands dimensions (~ 40 nm thick). We observe that the smallest potential shows the largest grain size, and at potentials more cathodic than -1.3V a steady decrease in grain size with voltage occurs. We also observe that after this critical potential of -1.3 V, the standard deviation of both the linewidth and frequency significantly increases. This increase in the standard deviation suggests that the grain size is less homogeneous when InAs is grown with larger potentials.

Discussion

Phonon confinement in seemingly large crystals can arise by a large defect density[32] and/or morphological features (e.g., nanostructured roughness). Both the increased grain size inhomogeneity and light-induced decomposition with deposition potential, seem to indicate that nanostructuring is the most plausible explanation to phonon confinement. To shed light on the origin of increased nanostructuring, we now introduce the model for the electro-chemically mediated InAs growth.

When As is electrochemically deposited on InAs/In, InAs growth will occur at two interfaces (As and In) through atom diffusion and solid-state reaction as shown in Figure 5a. At the As interface:

$$In(\text{diffusing}) + As(\text{surface}) \rightarrow InAs$$

and at the In interface:

$$As(\text{diffusing}) + In(\text{surface}) \rightarrow InAs$$

The InAs growth rate ($r_{InAs} = dx/dt$) due to the diffusion-reaction process has been extensively studied in non-electrochemical systems and can be estimated with the following expression:[33]

$$dx\left(\frac{x}{k_D}+\frac{1}{k_R}\right) = dt \qquad \text{Eq. 4}$$

where, k_R is the reaction rate constant and $\frac{k_D}{x}$ is the diffusional rate constant, where k_D is a physical constant that is

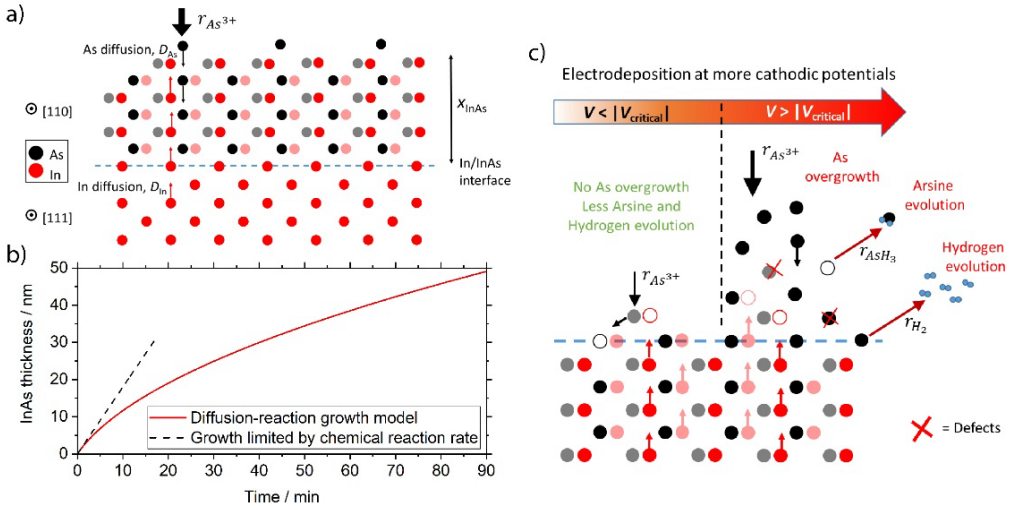

Figure 5. a) Illustrates the InAs growth mechanism during electrochemical deposition of As on an In foil. $r_{As^{3+}}$ is the potential-dependent As electrodeposition rate. b) InAs thickness temporal evolution based on Eq. 4, which deviates from the reaction limited regime (dashed line). We have used D =3.3x10^{-15} cm^2 s^{-1} and k_R= 3x10^{-9} cm s^{-1} (from Ref [18]) as parameters c) Illustration of the InAs growth mechanism below and above a critical potential ($V_{critical}$). In the illustrations a) and c) we have arbitrarily chosen the <110> InAs/<111> planes to represent a possible InAs/In epitaxial interface.. Circles shown with semitransparent colors correspond to atoms in a position slightly behind.

proportional to the diffusion coefficient (D) and the concentration gradient of the corresponding chemical species.

Regardless of which interface is contributing the most to the InAs growth, it is clear from Eq. 4 that for small InAs thicknesses (x), growth is limited by the reaction rate constant, k_R. On the other hand, after a certain thickness the diffusion rate $\left(\frac{k_D}{x}\right)$ will determine the overall growth.

Figure 5b shows the InAs thickness vs. time as predicted by Eq. 4 (solid line), assuming InAs growth to occur only at the In interface. The InAs thickness limited by the reaction rate is also shown as reference (dashed line). By comparing the two curves, it is clear that diffusion slows down the growth rate significantly already for InAs thicknesses as small as ~ 10 nm. Given the thickness of the InAs nano-islands in our samples, we suspect that growth is limited by self-diffusion and/or by the electrochemical deposition rate.

In electrochemical mediated growth, the concentration c of solid As at the surface is a function of the As^{3+} reduction rate ($r_{As^{3+}}$), which increases as the potential is made more cathodic. Figure 5c illustrates the role of potential in compromising crystallinity, based on the voltage-dependent local As deposition rate.

At small potentials, the electrochemical deposition of As^{3+} is slower than the diffusion of As atoms to the In interface, and no As overgrowth is expected. By contrast, if the rate of the As deposition is larger than that of the crystal growth, As will accumulate at the surface, enabling In diffusion and inhomogeneous InAs vertical growth. Additional to higher As deposition, large cathodic potentials may also increase the rate for arsine and hydrogen gas evolution. Both reactions can significantly increase the roughness/porosity of the film by (i) bubble formation, (ii) restriction of InAs growth in highly active sites for gas evolution, and, in the case of Arsine evolution, (iii) generation of As vacancies in already formed InAs.

Under our experimental conditions, we identify a critical potential to be -1.3 V, based on the rapid increase in phonon confinement after this potential value. The fact that InAs grown at potentials beyond the critical potential (i.e., -1.3V) exhibit the largest InAs decomposition when probed with a high intensity laser is in favour of the presence of nanostructured features (roughness/porosity).

Conclusions

To conclude, we have demonstrated that InAs nano-islands are formed when As is deposited on In at different cathodic potentials (-1.175 to -1.35 V). We show that the thickness of the InAs nano-islands grown in 90 min do not vary significantly with applied potential, suggesting that the growth is limited by diffusion of As atoms into the In, and not by the As ions' electrodeposition rate. While the nano-island thickness did not increase with potential, we find the resulting crystal quality to be significantly potential-dependent. Interestingly, the crystal correlation size of the InAs nano-islands at low applied potentials (~ 25 nm at -1.175 V) is almost as large as the nano-island thickness. Moreover, we show that for more cathodic potentials than a critical potential (i.e., -1.3 V) the crystal correlation size steadily decreases (i.e., to ~9 nm for -1.35 V). This clear grain size-potential relation can be used to electrochemically grow III-V nanostructures with predefined grain sizes. We assign the decrease in InAs crystal correlation size with applied potential to an increase in roughness due to (i) arsenic overgrowth and (ii) hydrogen/arsine gas evolution at more cathodic potentials.

While, we expect that a more homogenous deposition and growth (e.g., InAs films) can be achieved by changing other parameters (e.g., temperature), our results clearly show that the crystal properties are affected by the potential at room temperature. This opens up the possibility to vary crystal properties with the applied potential to tune the optoelectronic properties of the electrochemically grown III-V semiconductors at ambient temperatures and pressures.

Experimental

Chemicals and materials

The 0.127 mm thick In foil substrate (99.99% trace metal basis), Na_2SO_4 (>99.0%, anhydrous), NaOH (>98% anhydrous) and a As(III) standard solution for ICP (1000mg/L in HCL) were purchased from Merck.

Electrochemical methods

The CV and CA measurements were carried out with a SP-300 Bio-Logic potentiostat in a three-electrode configuration, where the working electrode area is fixed to 28.27 mm^2. A Pt wire was used as counter electrode, a Ag/AgCl electrode (leak less miniature ET072-1) was used as reference electrode and an In foil was used as working electrode. All measurements were carried out at pH 13 with a supporting electrolyte containing 0.1M Na_2SO_4 and 0.1M NaOH. For the experiments containing As ions, 0.78mM of As(III) was added to the solution. Since the As(III) precursor solution (see chemicals and materials section) used in this work contains HCl, ~ 32 mM of Cl- ions are also present in the electrolytes that contain As(III) ions. A water purification system from MIILLIPORE was used to demineralize the water (~18.2 MΩ cm) to prepare the electrolyte. The 3D design of the electrochemical cell used in this work is shown in Figure S9. Before every CA measurement three CV measurements were carried out between -0.6 to -1.7 V vs Ag/AgCl with an ending potential equal to ~ -1.12V vs. Ag/AgCl when going in the anodic direction. This ensures that the In surface is fully reduced after the CV measurements. Right after the end of the CV, the working electrode was kept at open circuit for 5 min before starting the CA at the potentials shown in Figure S2.

Raman spectroscopy

A WiTec α300SR confocal microscope equipped with a 100X ZEISS objective (EC Epiplan-Neofluar, HD M27, 0.9 NA, 0.28 mm working distance) was used to carry out the Raman spectroscopy measurements. The excitation 532 nm diode laser and the CCD (UHTS 300, WiTec) were used in a backscattering configuration. A 532 nm long pass filter (WiTec) was used to filter the excitation line. All spectra were corrected to match the Si Raman peak at 520 cm^{-1} of a reference bulk sample. The linewidths reported in Figure 4 are not limited by the resolution of the WiTec.

TO and LO Raman peaks fitting

The fitting of the measured LO and TO Raman peaks was carried out by optimizing the parameters of two Lorentzian functions (i.e., Lor_{TO} + Lor_{LO}) with the fminsearch tool of Matlab. For the TO peak (Lor_{TO}) the following symmetric Lorentzian function was used:

$$\mathrm{Lor} = \frac{2A/\pi\Gamma}{1+4[(\omega-\omega_0)/\Gamma]^2} \qquad \text{Eq. 5}$$

where, Γ is the linewidth, A is the peak area, ω is the Raman shift and ω_0 is the location of the peak maximum.

The LO peak was fitted with an asymmetric Lorentzian function,[34] where a frequency dependent Γ is introduced in Eq.5:

$$\Gamma(\omega) = \frac{2\Gamma_A}{1+\exp[a(\omega-\omega_A)]} \qquad \text{Eq. 6}$$

where a is the asymmetry parameter. It is worth highlighting that the optimized ω_A and Γ_A parameters are not the peak maximum and linewidth of the asymmetric fitted curve. The actual peak maximum and FWHM of the fit are the values reported in Figure 4b.

Conflicts of interest

There are no conflicts to declare

Acknowledgements

This work is part of the research program at the Netherlands Organisation for Scientific Research (NWO). Authors thank D. Ursem and the design and precision manufacturing departments at Amolf for their support.

Notes and references

1 H. Cotal, C. Fetzer, J. Boisvert, G. Kinsey, R. King, P. Hebert, H. Yoon and N. Karam, *Energy Environ. Sci.*, 2009, **2**, 174–192.

2 R. R. LaPierre, a. C. E. Chia, S. J. Gibson, C. M. Haapamaki, J. Boulanger, R. Yee, P. Kuyanov, J. Zhang, N. Tajik, N. Jewell and K. M. a. Rahman, *Phys. status solidi - Rapid Res. Lett.*, 2013, **7**, 815–830.

3 A. Polman, M. Knight, E. Garnett, B. Ehrler and W. C. Sinke, *Science (80-.).*, 2016, **352**, 1–24.

4 N. Tavakoli and E. Alarcon-Llado, *Opt. Express*, 2019, **27**, A909–A923.

5 R. J. Britto, J. L. Young, Y. Yang, M. A. Steiner, D. T. LaFehr, D. J. Friedman, M. Beard, T. G. Deutsch and T. F. Jaramillo, *J. Mater. Chem. A*, 2019.

6 M. M. May, H. Lewerenz, D. Lackner, F. Dimroth and T. Hannappel, *Nat. Commun.*, 2015, **6**, 1–7.

7 J. L. Young, K. X. Steirer, M. J. Dzara, J. A. Turner and T. G. Deutsch, *J. Mater. Chem. A*, 2016, **4**, 2831.

8 L. Shen, E. Y. B. Pun and J. C. Ho, *Mater. Chem. Front.*, 2017, **1**, 630–645.

9 R. R. Lapierre, M. Robson and P. Kuyanov, *J. Phys. D*, 2017, **50**, 123001.

10 J. A. Alexander-webber, C. K. Groschner, A. A. Sagade, G. Tainter, M. F. Gonzalez-zalba, R. Di Pietro, J. Wong-leung, H. H. Tan, C. Jagadish, S. Hofmann and H. J. Joyce, *ACS Appl. Mater. Interfaces*, 2017, **9**, 43993.

11 I. J. Luxmoore, R. Toro, O. Del Pozo-Zamudio, N. A. Wasley, E. A. Chekhovich, A. M. Sanchez, R. Beanland, A. M. Fox, M. S. Skolnick, H. Y. Liu and A. I. Tartakovskii, *Sci. Rep.*, 2013, **3**, 1239.

12 S. Dayeh, *Semicond. Sci. Technol.*, 2010, **25**, 024004.

13 S. A. Dayeh, D. P. R. Aplin, X. Zhou, P. K. L. Yu, E. T. Yu and D. Wang, *Small*, 2007, **3**, 326–332.

14 A. Y. Cho, *Thin Solid Films*, 1983, **100**, 291–317.

15 J. L. Shen, I. M. Chang, Y. M. Shu, Y. F. Chen, S. Z. Chang and S. C. Lee, *Phys. Rev. B*, 1994, **50**, 1678–1683.

16 K. Ploog and K. Graf, *Molecular Beam Epitaxy of III–V Compounds: A comprehensive bibliography*, Springer Berlin Heidelberg, Berlin, Heidelberg, 1980.

17 I. Garcia, B. Galiana, I. Rey-Stolle and C. Algora, in *2007 Spanish Conference on Electron Devices*, 2007, pp. 17–20.

18 E. Fahrenkrug, J. Gu and S. Maldonado, *Chem. Mater.*, 2014, **26**, 4535–4543.

19 E. Fahrenkrug, J. Gu and S. Maldonado, *J. Am. Chem. Soc.*, 2013, **135**, 330–339.

20 G. Hautier, K. Maex and P. M. Vereecken, *Electrochem. solid-state Lett.*, 2008, **11**, 47–49.

21 L. Wen, Z. Wang, Y. Mi, R. Xu, S.-H. Yu and Y. Lei, *Small*, 2015, **11**, 3408–28.

22 R. Carles, N. Saint-Cricq, J. B. Renucci, M. A. Renucci and A. Zwick, *Phys. Rev. B*, 1980, **22**, 4804–4815.

23 J. S. Lannin, *Phys. Rev. B*, 1977, **15**, 3863–3871.

24 J. He, P. Chen, W. Lu, N. Dai and D.-M. Zhu, *Appl. Phys. A*, 2014, **115**, 885–893.

25 R. Tanta, T. Kanne, F. Amaduzzi, Z. Liao, M. Madsen, E. Alarcon-llado, P. Krogstrup, E. Johnson, A. Fontcuberta I Morral, T. Vosch and T. Jespersen, *Nanotechnology*, 2016, **27**, 1–8.

26 P. N. Martin, Z. Aksamija, E. Pop and U. Ravaioli, *Nano Lett.*, 2010, **10**, 1120–1124.

27 M. Soini, I. Zardo, E. Uccelli, S. Funk, G. Koblmüller, A. Fontcuberta and G. Abstreiter, *Appl. Phys. Lett.*, 2010, **97**, 263107.

28 R. S. Frederiksen, E. Alarcon-Llado, M. H. Madsen, K. R. Rostgaard, P. Krogstrup, T. Vosch, J. Nygård, A. Fontcuberta I Morral and K. L. Martinez, *Nano Lett.*, 2015, **15**, 176–181.

29 P. M. Wu, N. Anttu, H. Q. Xu, L. Samuelson and M. Pistol, *Nano Lett*, 2012, **12**, 1990.

30 R. Tanta, C. Lindberg, S. Lehmann, J. Bolinsson, M. R. Carro-Temboury, K. A. Dick, T. Vosch, T. S. Jespersen and J. Nygård, *Phys. Rev. B*, 2017, **96**, 165433.

31 P. Parayanthal and F. H. Pollak, *Phys. Rev. Lett.*, 1984, **52**, 1822–1825.

32 K. K. Tiong, P. M. Amirtharaj, F. H. Pollak and D. E. Aspnes, *Appl. Phys. Lett.*, 1984, **44**, 122–124.

33 V. I. Dybkov, *J. Mater. Sci.*, 1986, **21**, 3078–3084.

34 A. L. Stancik and E. B. Brauns, *Vib. Spectrosc.*, 2008, **47**, 66–69.